

Near-infrared spectroscopy of a large sample of low-metallicity blue compact dwarf galaxies

Y. I. Izotov¹ and T. X. Thuan²

¹*Main Astronomical Observatory, Ukrainian National Academy of Sciences, Zabolotnoho 27, Kyiv 03680, Ukraine*

²*Astronomy Department, University of Virginia, P.O. Box 400325, Charlottesville, VA 22904-4325*

20 August 2021

ABSTRACT

We present near-infrared (NIR) spectroscopic observations in the wavelength range $0.90\mu\text{m}$ – $2.40\mu\text{m}$ of eighteen low-metallicity blue compact dwarf (BCD) galaxies and six H II regions in spiral and interacting galaxies. Hydrogen and helium emission lines are detected in all spectra, while H₂ and iron emission lines are detected in most spectra. The NIR data for all objects have been supplemented by optical spectra. In all objects, except perhaps for the highest metallicity ones, we find that the extinctions $A(V)$ in the optical and NIR ranges are similar, implying that the NIR hydrogen emission lines in low-metallicity BCDs do not reveal more star formation than seen in the optical. We conclude that emission-line spectra of low-metallicity BCDs in the ~ 0.36 – $2.40\mu\text{m}$ wavelength range are emitted by a relatively transparent ionized gas. The H₂ emission line fluxes can be accounted for by fluorescence in most of the observed galaxies. We find a decrease of the H₂ 2.122 μm emission line relative to the Br γ line with increasing ionization parameter. This indicates an efficient destruction of H₂ by the stellar UV radiation. The intensities of the [Fe II]1.257 μm and 1.644 μm emission lines in the spectra of all galaxies, but one, are consistent with the predictions of Cloudy stellar photoionization models. There is thus no need to invoke shock excitation for these lines, and they are not necessarily shock indicators in low-metallicity high-excitation BCDs. The intensity of the He I 2.058 μm emission line is lower in high-excitation BCDs with lower neutral gas column densities and higher turbulent motions.

Key words: galaxies: dwarf – galaxies: starburst – galaxies: ISM – galaxies: abundances.

1 INTRODUCTION

Blue compact dwarf (BCD) galaxies have oxygen abundances that vary in the range $12 + \log \text{O}/\text{H} = 7.1 - 8.3$, i.e. $1/45 - 1/3$ that of the Sun, if the solar abundance of Steffen et al. (2015), $12 + \log \text{O}/\text{H} = 8.76$, is adopted. They thus constitute excellent nearby laboratories for studying star formation and its interaction with the interstellar medium (ISM) in a metal-deficient environment (see Thuan 2008, for a review). They are also of cosmological interest because, besides having low metallicities, they are also compact, have low-mass (10^8 – $10^9 M_{\odot}$), high specific star formation rates, high gas masses and clumpy morphologies, making them the best local proxies for high-redshift Lyman alpha emitting galaxies which also share these properties.

While BCDs have been extensively studied spectroscopically in the optical range, not much recent work has been done in the near-infrared (NIR) $0.9 - 2.4 \mu\text{m}$ range. We have started a long-term observational program to study the NIR spectroscopic properties of a sample of BCDs cho-

sen to cover a large range of metallicities. The first results of the program, concerning six BCDs, have been discussed by Izotov, Thuan & Wilson (2009) and Izotov & Thuan (2011). Here, we present new J , H and K spectroscopic observations of eighteen more low-metallicity BCDs as well as of H II regions J0115–0051, UM 311, Mrk 1089, Mrk 94, J1038+5330, and Mrk 1315 in the spiral or interacting galaxies with slightly higher metallicities. The $12 + \log \text{O}/\text{H}$ of the objects in the sample ranges from 7.25 to 8.40.

In this new sample, only a few galaxies have had previous NIR spectral observations. However, all these spectra covered a more restricted wavelength range, including only either the H band and/or the K band, with generally a lower signal-to-noise ratio. The general characteristics of all 24 objects are given in Table 1. With the TripleSpec spectrograph at the Apache Point Observatory (APO) 3.5-meter

Table 1. General characteristics of galaxies

Object	R.A. (J2000.0)	Dec. (J2000.0)	g, B	M_g, M_B	Redshift	12+logO/H	Comments
HS 0021+1347	00 24 25.9	+14 04 10	15.86	-17.81	0.01423	8.39 [‡]	BCD
J0115-0051	01 15 33.8	-00 51 31	16.51	-14.85	0.00559	8.37 [‡]	H II region in spiral galaxy
UM 311	01 15 34.4	-00 51 46	17.90	-13.46	0.00559	8.33 [‡]	H II region in spiral galaxy
SHOC 137	02 48 15.8	-08 17 24	16.29	-14.04	0.00469	7.97 [‡]	BCD
Mrk 600	02 51 04.6	+04 27 14	15.45 [†]	-14.73	0.00336	7.79*	BCD
Mrk 1089	05 01 37.7	-04 15 28	13.40 [†]	-20.32	0.01341	8.00*	interacting galaxies
Mrk 94	08 37 43.5	+51 38 30	16.90	-13.50	0.00244	8.08 [‡]	H II region in spiral galaxy
I Zw 18	09 34 02.0	+55 14 28	16.08 [†]	-14.39	0.00251	7.24 [‡]	BCD
CGCG 007-025	09 44 01.9	-00 38 32	16.05	-15.91	0.00483	7.77 [‡]	BCD
J1038+5330	10 38 44.8	+53 30 05	13.15	-17.82	0.00320	8.30 [‡]	H II region in spiral galaxy
Haro 3	10 45 22.4	+55 57 37	13.25 [†]	-17.67	0.00315	8.35 ^{‡*}	BCD
Mrk 36	11 04 58.3	+29 08 23	15.70 [†]	-14.87	0.00216	7.83 [‡]	BCD
Mrk 162	11 05 08.1	+44 44 47	14.93	-19.92	0.02154	8.22 [‡]	BCD
Mrk 1450	11 38 35.7	+57 52 27	15.29	-15.61	0.00316	8.11*	BCD
Mrk 193	11 55 28.3	+57 39 52	16.40	-17.94	0.01720	7.93 [‡]	BCD
Mrk 1315	12 15 18.6	+20 38 27	16.27	-14.75	0.00283	8.33 [‡]	H II region in spiral galaxy
SBS 1222+614	12 25 05.4	+61 09 11	14.72	-15.58	0.00236	8.01 [‡]	BCD
Mrk 209	12 26 15.9	+48 29 37	15.13	-13.96	0.00094	7.88 [‡]	BCD
Mrk 1329	12 37 03.0	+06 55 36	14.40 [†]	-17.76	0.00544	8.34 [‡]	BCD
Mrk 450	13 14 48.3	+34 52 51	14.30 [†]	-16.59	0.00288	8.16 [‡]	BCD
Mrk 259	13 28 44.0	+43 55 51	16.27	-19.13	0.02795	8.11 [‡]	BCD
SBS 1415+437	14 17 01.4	+43 30 05	15.68 [†]	-14.42	0.00203	7.57*	BCD
Mrk 475	14 39 05.4	+36 48 22	15.46 [†]	-14.57	0.00195	7.93 [‡]	BCD
Mrk 487	15 37 04.2	+55 15 48	15.45 [†]	-14.50	0.00222	8.06 [‡]	BCD

[†] B magnitude. In all other cases, the g magnitude is given.

[‡]SDSS spectrum is used for oxygen abundance determination.

*3.5m APO spectrum is used for oxygen abundance determination.

^{‡*}SDSS spectrum of the Haro 3 center and 3.5m APO spectrum of the offset H II region are used for oxygen abundance determination. Oxygen abundance is for the galaxy center.

telescope¹, we can obtain NIR spectra with a simultaneous coverage of the JHK bands and significantly more signal-to-noise ratio than previous spectra. These improved observations will allow us to study in more detail the physical conditions in H II regions. The considerably larger sample will also permit us to check for the dependence of various physical parameters on metallicity. We will be able to compare the extinctions in the optical and NIR and search for hidden star formation. We will also be able to study the excitation mechanisms of line emission of ionized species in the H II regions, and search for molecular hydrogen emission.

We describe the 3.5m APO observations in Section 2. In Section 3, we discuss their extinction, both in the optical and NIR ranges, the excitation mechanisms for molecular hydrogen and iron emission in the NIR range. We also examine how the intensity of the He I $\lambda 2.058\mu\text{m}$ emission depends on various physical conditions. We summarize our findings in Section 4.

2 OBSERVATIONS

2.1 Near-infrared observations

NIR spectra were obtained with the 3.5 m APO telescope, equipped with the TripleSpec spectrograph, on different nights during the 2010-2013 period. TripleSpec

(Wilson et al. 2004) is a cross-dispersed NIR spectrograph that provides simultaneous continuous wavelength coverage from 0.90 to 2.46 μm in five spectral orders during a single exposure. A $1''1 \times 43''$ slit was used, resulting in a resolving power of 3500. While the present sample contains 24 objects, there are two galaxies, Haro 3 and Mrk 1089, for which spectra were obtained for two different star-forming regions within the same object. We therefore analyze a total of 26 NIR spectra.

Several A0V standard stars at airmasses close to those of the objects were observed for flux calibration and correction for telluric absorption. Spectra of Ar comparison arcs were obtained on the same date for wavelength calibration. Since all observed targets are smaller than the length of the slit, the nod-on-slit technique was used to acquire the sky spectrum. Objects were observed by nodding between two positions A and B along the slit, following the ABBA sequence, and with an integration time of 200s or 300s at each position.

We carried out the reduction of the data according to the following procedures. The two-dimensional spectra were first cleaned for cosmic ray hits using the IRAF² routine CR-MEDIAN. Then all A and B frames were separately coadded

¹ The Apache Point Observatory 3.5-meter telescope is owned and operated by the Astrophysical Research Consortium.

² IRAF is the Image Reduction and Analysis Facility distributed by the National Optical Astronomy Observatory, which is operated by the Association of Universities for Research in Astronomy (AURA) under cooperative agreement with the National Science Foundation (NSF).

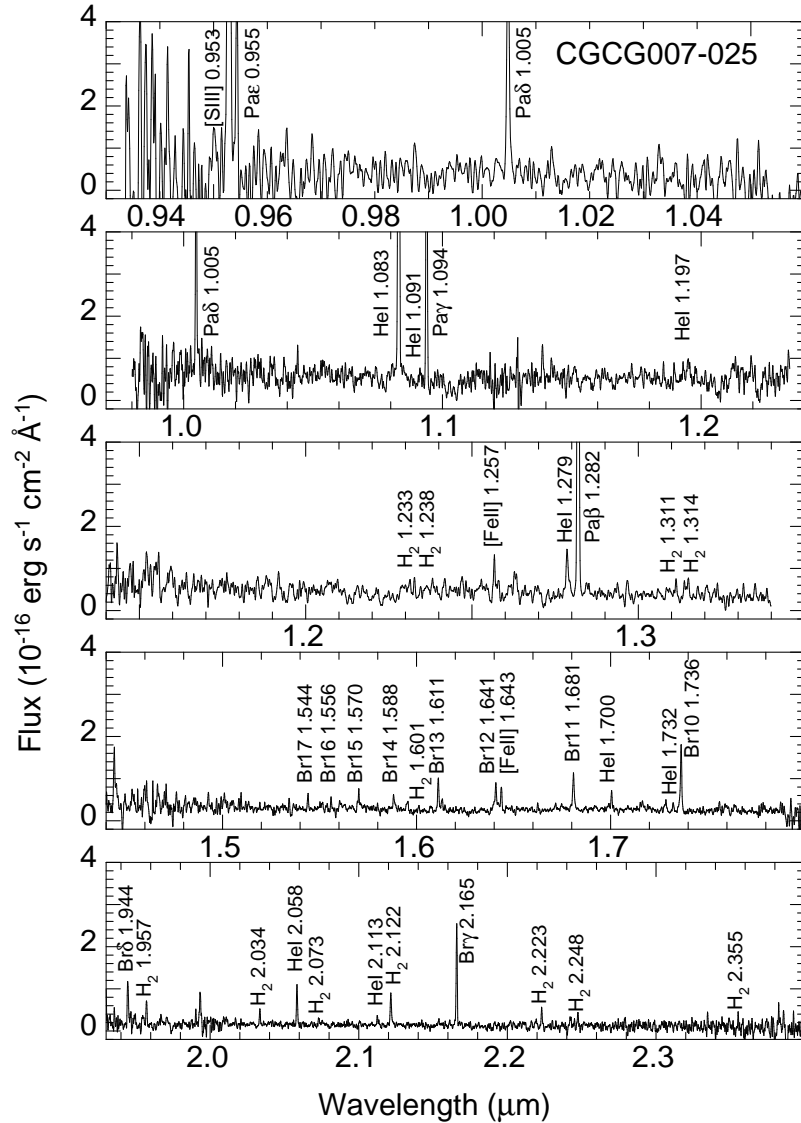


Figure 1. As an example of the 3.5m APO/TripleSpec NIR spectra of BCDs, we show the redshift-corrected spectrum of CGCG007-025 which shows numerous H₂ emission lines, along with hydrogen, helium and [Fe II] lines.

and the resulting B frame was subtracted from the resulting A frame. This procedure is equivalent to subtracting each A frame from its time-adjacent B frame and then coadding all difference frames. However, some background residuals still remain in the coadded spectra because of the sky background short-time variations. Finally, the (negative) spectrum at position B was adjusted to the (positive) spectrum at position A and subtracted from it. At this stage, the remaining background residuals are nearly totally eliminated and the signal-to-noise ratio of the final positive spectrum of the object is increased by a factor of $\sqrt{2}$ because of coadding of the exposures at positions A and B. The same reduction scheme was applied to the standard stars.

We then use the IRAF routines IDENTIFY, REIDENTIFY, FITCOORD, TRANSFORM to perform wavelength calibration and correction for distortion and tilt for each frame. A one-dimensional spectra of all galaxies were ex-

tracted from the two-dimensional frames using the APALL IRAF routine, within a $1'' \times 6''$ rectangular aperture so as to include the brightest star-forming regions.

Flux calibration and correction for telluric absorption were performed by first multiplying the one-dimensional spectrum of each galaxy by the synthetic absolute spectral distributions of standard stars, smoothed to the same spectral resolution, and then by dividing the result by the observed one-dimensional spectrum of the same star. Since there does not exist any published absolute spectral energy distribution of standard stars, we have derived them by scaling the synthetic absolute spectral energy distribution of the star Vega (α Lyrae), of similar spectral type A0V, to the brightness of the telluric standard.

As an example, the resulting one-dimensional flux-calibrated and redshift-corrected NIR spectrum of the BCD

Table 2. Extinction-corrected fluxes of strong hydrogen lines

Line	Galaxy						
	HS0021+1347	J0115–0051	UM311	SHOC137	Mrk600	Mrk1089#1	Mrk1089#2
0.410 H δ	25.9	27.2	23.9	26.8	22.3	22.2	22.7
0.434 H γ	46.8	48.7	48.6	52.1	50.3	49.9	51.0
0.434 H β	100.0	100.0	100.0	100.0	100.0	100.0	100.0
0.656 H α	289.6	292.9	290.1	284.9	281.7	292.3	293.4
1.094 P γ	7.6	7.6	9.1	7.8	11.4	7.9	7.2
1.282 P β	16.6	12.2	18.2	15.2	20.2	16.2	15.8
2.165 Br γ	2.9	2.1	2.1	2.8	2.9	3.1	2.4
Line	Mrk94	IZw18	CGCG007-025	J1038+5330	Haro3#1	Haro3#2	Mrk36
0.410 H δ	25.7	25.2	25.6	26.3	25.9	25.0	26.6
0.434 H γ	49.0	48.4	49.3	47.7	47.3	47.6	47.4
0.434 H β	100.0	100.0	100.0	100.0	100.0	100.0	100.0
0.656 H α	287.1	279.2	284.0	296.1	291.4	293.3	281.9
1.094 P γ	13.7	6.4	8.0	10.5	8.2	9.4	9.5
1.282 P β	23.8	10.1	13.0	17.3	13.5	15.2	14.3
2.165 Br γ	3.4	1.9	2.7	2.8	2.8	3.7	1.9
Line	Mrk162	Mrk1450	Mrk193	Mrk1315	SBS1222+614	Mrk209	Mrk1329
0.410 H δ	26.7	25.6	26.6	26.4	27.5	28.4	28.2
0.434 H γ	48.5	47.5	47.5	47.1	49.3	50.7	50.3
0.434 H β	100.0	100.0	100.0	100.0	100.0	100.0	100.0
0.656 H α	290.6	286.7	286.1	288.7	284.9	284.2	292.7
1.094 P γ	7.8	9.7	7.0	10.3	8.1	8.6	9.8
1.282 P β	12.3	13.1	13.2	15.6	14.9	14.9	14.0
2.165 Br γ	2.8	3.2	2.8	3.9	2.6	2.5	3.1
Line	Mrk450	Mrk259	SBS1415+437	Mrk475	Mrk487	Case B ^a	
0.410 H δ	30.4	25.7	27.3	26.2	19.6	26.2	
0.434 H γ	51.7	47.5	47.7	46.2	31.7	47.3	
0.434 H β	100.0	100.0	100.0	100.0	100.0	100.0	
0.656 H α	291.7	288.2	283.8	277.3	283.4	279.0	
1.094 P γ	9.7	9.9	6.9	6.3	6.7	8.6	
1.282 P β	13.6	16.7	13.4	11.3	13.0	15.2	
2.165 Br γ	2.9	3.1	2.5	1.7	2.5	2.5	

^aRecombination ratios for $T_e=15000$ K and $N_e = 100 \text{ cm}^{-3}$ from Storey & Hummer (1995).

CGCG 007-025 is shown in Fig. 1. Strong hydrogen and helium lines and numerous H₂ emission lines are seen.

2.2 Optical data

To have a more complete physical picture of the extinction and of the ionization mechanisms in our galaxies, we have supplemented the NIR observations with optical ones. Sloan Digital Sky Survey (SDSS) spectra are available for all galaxies, except for four objects: Mrk600, Mrk 1089, SBS 1415+437, and an offset H II region in Haro 3. Additionally, one object, Mrk 1450, does have a SDSS spectrum, but all strong lines are clipped in that spectrum, making it unusable. Furthermore, since our galaxies are at low redshifts, the [O II] $\lambda 0.373 \mu\text{m}$ emission line is not in the observed spectral range of their SDSS spectra, except for the SDSS spectrum of Mrk 259. This line is essential for accurate abundance determinations. Therefore, we have obtained our own optical observations for most galaxies with the 3.5 m APO telescope, during the course of several nights in the period 2010 – 2013. This allows us to obtain spectra for the 5 ob-

jects with no SDSS data, and intensities of the [O II] $\lambda 0.373 \mu\text{m}$ emission line for most objects.

The 3.5 m APO observations were made with the Dual Imaging Spectrograph (DIS) in both the blue and red wavelength ranges. In the blue range, we use the B400 grating with a linear dispersion of $1.83 \times 10^{-4} \mu\text{m}/\text{pix}$ and a central wavelength of $0.44 \mu\text{m}$, while in the red range we use the R300 grating with a linear dispersion $2.31 \times 10^{-4} \mu\text{m}/\text{pix}$ and a central wavelength of $0.75 \mu\text{m}$. The above instrumental setup gave a spatial scale along the slit of $0''.4 \text{ pixel}^{-1}$, a spectral range $\sim 0.36 - 0.97 \mu\text{m}$ and a spectral resolution of $7 \times 10^{-4} \mu\text{m}$ (FWHM). Several Kitt Peak IRS spectroscopic standard stars were observed for flux calibration. Spectra of He-Ne-Ar comparison arcs were obtained at the beginning or the end of each night for wavelength calibration. However, we do not have APO observations for CGCG 007-025, UM 311, Mrk 94, SHOC 137, HS 0021+1347, SBS 1222+614, Mrk 162, and J1038+5330. In those cases, we adopted the [O II] $\lambda 0.373 \mu\text{m}$ intensities from Guseva et al. (2007) for CGCG 007-025, SHOC 137 and UM 311, from Thuan & Izotov (2005) for Mrk 94, from Izotov, Thuan & Lipovetsky (1997) for SBS 1222+614, and from Izotov & Thuan (1998) for Mrk 162. For the remaining galaxies, HS 0021+1347 and J1038+5330,

the [O II] $\lambda 0.373\mu\text{m}$ line intensities were calculated from the [O II] $\lambda 0.720\mu\text{m}$, $\lambda 0.730\mu\text{m}$ doublet in the SDSS spectra.

The two-dimensional optical spectra were bias subtracted and flat-field corrected using IRAF. We then use the IRAF software routines IDENTIFY, REIDENTIFY, FITCOORD, TRANSFORM to perform wavelength calibration and correction for distortion and tilt for each frame. One-dimensional spectra were then extracted from each frame using the APALL routine. The sensitivity curve was obtained by fitting with a high-order polynomial the observed spectral energy distribution of standard stars. Then sensitivity curves obtained from observations of different stars during the same night were averaged.

With the [O II] $\lambda 0.373\mu\text{m}$ line intensity measured from the APO/DIS spectra, we have used the SDSS spectra whenever available and APO spectra otherwise to derive the physical conditions and oxygen abundances of all objects, following the procedures described by Izotov et al. (2006). The APO spectrum was used for Mrk 1450 because of the clipping problem in the SDSS spectrum. We have preferred to use SDSS instead of APO spectra because they are available for 20 out of 24 galaxies in our sample. Furthermore, they have a reliable spectrophotometric flux calibration, giving accurate absolute emission-line fluxes. On the other hand, only 16 galaxies in our sample possess APO/DIS spectra, many of which were obtained in non-photometric conditions, introducing uncertainties in the absolute flux calibration. The derived oxygen abundances are shown in Table 1. The combination of observations obtained with different telescopes and varying spectroscopic apertures may introduce uncertainties in those abundances. We estimate these uncertainties by comparing the oxygen abundances derived here with those by Izotov, Thuan & Guseva (2014). They have compiled oxygen abundance determinations for many objects in our sample (see their Table 1). It can be seen that, on average, the differences between the oxygen abundances in this paper and those in Table 1 of Izotov et al. (2014) are $\lesssim 0.05$ dex. This accuracy is quite sufficient for our purposes here. On the other hand, extinction coefficients do not suffer from this effect since hydrogen line ratios are derived from a single spectrum obtained with a single telescope.

We have adjusted the flux levels of the optical and NIR spectra by scaling the fluxes of the [S III] $\lambda 0.907\mu\text{m}$ emission line in the optical spectrum and the [S III] $\lambda 0.953\mu\text{m}$ emission line in the NIR spectrum, so that their ratio is equal to the theoretical line ratio $\lambda 0.953\mu\text{m}/\lambda 0.907\mu\text{m}$ of 2.486 (Aller 1984). These two lines are close enough in wavelength so that differential extinction can be neglected. This procedure could not be applied to two galaxies, Mrk 162 and Mrk 259, the objects with the highest redshifts in our sample. In these cases, the [S III] $\lambda 0.907\mu\text{m}$ emission line is shifted out of the SDSS spectral range, so that the adjustment of optical and NIR spectra, using the [S III] emission lines, was not possible. The optical and NIR flux levels of the spectra of these two galaxies were adjusted by matching their continuum fluxes in the overlapping spectral range.

3 RESULTS AND DISCUSSION

Emission-line fluxes in both the optical and NIR ranges were measured by using the SPLIT routine in IRAF. The errors

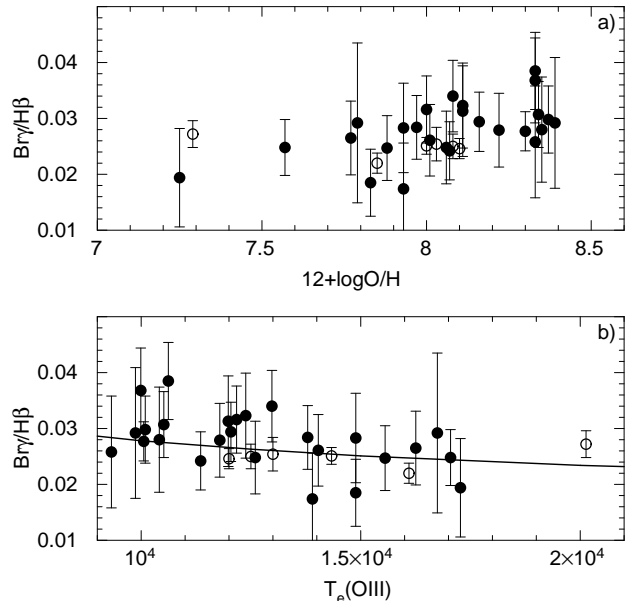


Figure 2. The $\text{Br}\gamma/\text{H}\beta$ flux ratio as a function of (a) the oxygen abundance $12 + \log \text{O}/\text{H}$ and (b) the electron temperature $T_e(\text{O III})$ derived from the $[\text{O III}]\lambda 0.436/(\lambda 0.496 + \lambda 0.507)$ flux ratio. The data from this paper and from our previous work (Izotov et al. 2009; Izotov & Thuan 2011) are shown respectively by filled and open circles. The solid line in (b) shows the theoretical case B recombination ratio calculated by Storey & Hummer (1995).

of the line fluxes were calculated from the photon statistics in the non-flux-calibrated spectra. For most of our galaxies, we have added the errors due to the adjustment of the optical and NIR spectra to the errors of the NIR lines, using the uncertainties in the [S III] $\lambda 0.907\mu\text{m}$ and [S III] $\lambda 0.953\mu\text{m}$ emission-line fluxes. This procedure did not apply to the two objects where the continuum adjustment was not done with the [S III] lines, Mrk 162 and Mrk 259. Here, we have added the uncertainties of the continuum placement to the errors of the NIR lines. The emission-line measurements from the adjusted optical and NIR spectra are shown in Tables 2 – 4. Table 2 gives the extinction-corrected fluxes of strong hydrogen lines. Table 3 represents the H_2 emission-line flux ratios and Table 4 lists the fluxes of the strongest [Fe II] emission lines. All line fluxes are normalized to the $\text{H}\beta$ flux.

The presence of many emission lines in the optical and NIR spectra allows us to study extinction, H_2 and [Fe II] emission and excitation mechanisms, and He I emission in galaxies. Combining our present sample of 18 BCDs and 6 H II regions in spiral and interacting galaxies with our previous samples containing 6 BCDs (Izotov et al. 2009; Izotov & Thuan 2011), we have a total sample of 30 objects, large enough to examine various statistical trends. We discuss these issues in the following sections.

3.1 Optical and NIR extinction and hidden star formation

In previous optical-NIR studies of BCDs, except for our own work (Izotov et al. 2009; Izotov & Thuan 2011), *JHK* spectra have been observed separately, and there has been no wavelength overlap between the optical and NIR spectra.

Table 3. H₂ emission-line flux ratios relative to the H₂ λ 2.122 μ m flux

Line	Galaxy						
	HS0021+1347	J0115-0051	UM311	SHOC137	Mrk600	Mrk1089#1	Mrk1089#1
1.233 H ₂ 3-1 S(1)	...	0.4
1.238 H ₂ 2-0 Q(1)	...	0.6
1.957 H ₂ 1-0 S(3)	...	0.3
2.034 H ₂ 1-0 S(2)	...	0.5	0.5	0.6	0.5
2.073 H ₂ 2-1 S(3)	...	0.3	0.3	0.4
2.122 H ₂ 1-0 S(1)	...	1.0	1.0	1.0	1.0	1.0	1.0
2.223 H ₂ 1-0 S(0)	...	0.4	0.5	0.4
2.248 H ₂ 2-1 S(1)	...	0.4	0.5	0.4
Line	Mrk94	IZw18	CGCG007-025	J1038+5330	Haro3#1	Haro3#2	Mrk36
1.233 H ₂ 3-1 S(1)	0.3	0.9	...
1.238 H ₂ 2-0 Q(1)	0.3	0.7	...
1.311 H ₂ 4-2 S(1)	0.3
1.314 H ₂ 3-1 Q(1)	0.3
1.601 H ₂ 6-4 Q(1)	0.2	0.2	...
1.957 H ₂ 1-0 S(3)	0.6
2.034 H ₂ 1-0 S(2)	0.3	0.5	...
2.073 H ₂ 2-1 S(3)	0.1	...	0.4	0.3	...
2.122 H ₂ 1-0 S(1)	1.0	1.0	1.0	1.0	1.0
2.223 H ₂ 1-0 S(0)	0.6	...	0.6	0.3	...
2.248 H ₂ 2-1 S(1)	0.4	...	0.6	0.5	...
2.355 H ₂ 2-1 S(0)	0.3
Line	Mrk162	Mrk1450	Mrk193	Mrk1315	SBS1222+614	Mrk209	Mrk1329
1.957 H ₂ 1-0 S(3)	0.9
2.034 H ₂ 1-0 S(2)	0.3	0.7	...	0.5	...	0.8	...
2.073 H ₂ 2-1 S(3)	...	0.5	...	0.7
2.122 H ₂ 1-0 S(1)	1.0	1.0	1.0	1.0	1.0	1.0	1.0
2.223 H ₂ 1-0 S(0)	0.2
2.248 H ₂ 2-1 S(1)	0.5
Line	Mrk450	Mrk259	SBS1415+437	Mrk475	Mrk487	Fluor ^a	Coll ^a
1.233 H ₂ 3-1 S(1)	0.7	0.5	0.0
1.238 H ₂ 2-0 Q(1)	0.5	0.4	0.0
1.311 H ₂ 4-2 S(1)	0.4	0.0
1.314 H ₂ 3-1 Q(1)	0.6	0.0
1.601 H ₂ 6-4 Q(1)	0.4	0.0
1.957 H ₂ 1-0 S(3)	0.9
2.034 H ₂ 1-0 S(2)	0.5	...	0.4	0.5	0.3
2.073 H ₂ 2-1 S(3)	0.2	0.2	0.0
2.122 H ₂ 1-0 S(1)	1.0	1.0	1.0	1.0	1.0	1.0	1.0
2.223 H ₂ 1-0 S(0)	0.3	...	0.5	0.6	0.3
2.248 H ₂ 2-1 S(1)	0.4	0.5	0.0
2.355 H ₂ 2-1 S(0)	0.6	0.3	0.0

^aModel values are from Black & van Dishoeck (1987). We adopt their model 1 for fluorescent lines and model S1 for collisionally excited lines.

This introduces uncertainties, due to the use of generally different apertures in the optical and NIR observations, and due to the adjusting of the continuum levels of NIR spectra obtained separately in different orders. Because our NIR spectra have been obtained simultaneously over the whole *JHK* wavelength range and because it is possible to directly match the optical and NIR spectra using [S III] emission line fluxes, these adjusting uncertainties are strongly reduced. This allows us to directly compare the optical and NIR extinctions and search for any hidden extinction at longer wavelengths. For comparison, the last column at the bottom of Table 2 shows the theoretical recombination flux ratios, calculated by Storey & Hummer (1995) for case B, with an

electron temperature $T_e = 15000$ K and an electron number density $N_e = 100$ cm⁻³. It can be seen that there is general agreement between the corrected and theoretical recombination values of both optical and NIR line fluxes. Therefore the same extinction coefficient $C(H\beta)$ [or $A(V)$] holds over the whole 0.36 – 2.40 μ m wavelength range, implying that there is no appreciable hidden star formation in the NIR as compared to in the optical range. This appears to be a general result for BCDs (e.g. Vanzi et al. 2000; Vanzi, Hunt & Thuan 2002; Izotov et al. 2009; Izotov & Thuan 2011).

Since the amount of dust may be related to the metallicity of the galaxy, one may ask whether there is a correlation between the metallicity of the galaxy and its extinc-

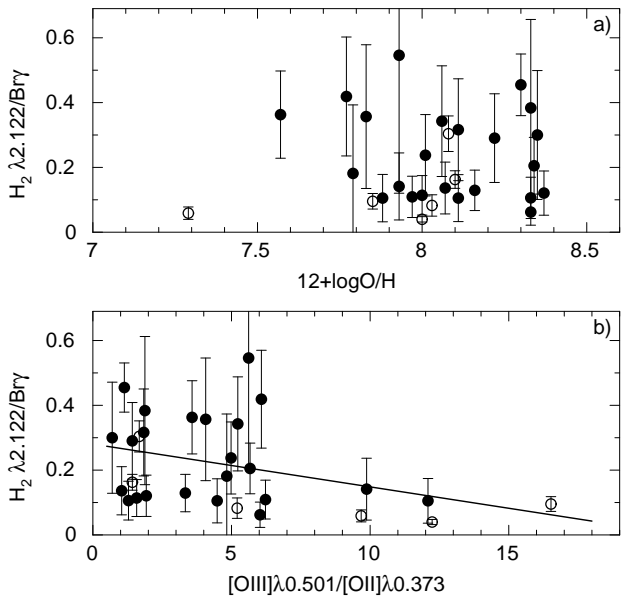


Figure 3. Plots of the $\text{H}_2 \lambda 2.122/\text{Br}\gamma$ flux ratio as a function of (a) the oxygen abundance $12+\log\text{O}/\text{H}$ and (b) the $[\text{O III}]\lambda 0.501/[\text{O II}]\lambda 0.373$ flux ratio. The meaning of the symbols is the same as in Fig. 2. The linear regression in (b) is shown by the solid line.

tion, as measured by the observed $\text{Br}\gamma/\text{H}\beta$ flux ratio. In Fig. 2a, we plot the $\text{Br}\gamma/\text{H}\beta$ flux ratio against the oxygen abundance $12+\log\text{O}/\text{H}$, using the present data (filled circles) and that of Izotov et al. (2009) and Izotov & Thuan (2011) (open circles). There is a weak trend in the sense of larger $\text{Br}\gamma/\text{H}\beta$ for higher oxygen abundances. However, the theoretical case B $\text{Br}\gamma/\text{H}\beta$ flux ratio does not depend directly on the oxygen abundance, but on the electron temperature, which is higher in low-metallicity galaxies. Therefore we show in Fig. 2b the dependence of the $\text{Br}\gamma/\text{H}\beta$ flux ratio on the electron temperature $T_e(\text{O III})$, as derived from the $[\text{O III}]\lambda 0.436/(\lambda 0.496+\lambda 0.507)$ flux ratio. The solid line indicates the theoretical case B ratio calculated by Storey & Hummer (1995). It is seen that the $\text{Br}\gamma/\text{H}\beta$ flux ratio is generally consistent with the case B values. However, there appears to be a slight systematic excess for galaxies with cool (and hence higher-metallicity) H II regions having $T_e(\text{O III}) < 13000$ K, indicating perhaps a small contribution from star-forming regions that are hidden in the optical range but seen in the NIR range. But overall, we may conclude that low-metallicity BCDs are transparent, in agreement with previous studies by Izotov et al. (2009) and Izotov & Thuan (2011).

3.2 H_2 emission

Molecular hydrogen lines do not originate in the H II region, but in neutral molecular clouds. In the NIR, they are excited by two mechanisms. The first one is the thermal mechanism consisting of collisions between neutral species (e.g., H , H_2), resulting from large-scale shocks driven by powerful stellar winds, supernova remnants or molecular cloud collisions. The second one is the fluorescent mechanism due to absorption of ultraviolet photons. It is known that these two mech-

anisms excite mostly different roto-vibrational levels of H_2 . By comparing the observed line ratios with those predicted by models such as those calculated by Black & van Dishoeck (1987), it is possible to discriminate between the two processes. In particular, line emission from the vibrational level $v=2$ and higher vibrational levels are virtually absent in collisionally excited spectra, while they are relatively strong in fluorescent spectra.

H_2 emission lines are detected in 23 NIR spectra of 21 objects (Mrk 1089 and Haro 3 have two spectra each, Table 3), but they are not seen in the spectra of HS0021+1347, I Zw 18 and Mrk 94, possibly because of the weakness of these lines and spectra with insufficient signal-to-noise ratio. This corresponds to a H_2 detection rate of 88% for our sample. We note that Hunt et al. (2010) also detected with mid-infrared Spitzer/IRS observations rotational transitions of H_2 in the warm neutral phase of the ISM of more than a third of their sample of 22 BCDs. Although this H_2 detection rate is lower than ours because of the lower signal-to-noise ratio of the IRS spectra, the Spitzer data also show that H_2 molecules are present in the warm neutral phase of the ISM of BCDs.

Four objects in our total BCD sample – I Zw 18, Mrk 209=I Zw 36, Mrk 59 and SBS 0335–052E – have also been observed by the Far Ultraviolet Spectroscopic Explorer (FUSE) satellite in an attempt to detect H_2 in absorption spectra. However, none showed H_2 absorption lines (e.g. Thuan, Lecavelier des Etangs & Izotov 2005). Yet, except for I Zw 18, the other three BCDs all show H_2 NIR emission lines (Mrk 59, SBS 0335–052E, Izotov et al. 2009; Izotov & Thuan 2011, and Mrk 209, this paper). The absence of H_2 absorption lines in FUSE spectra implies that the warm H_2 detected through IR emission must be quite clumpy. The FUSE observations are not sensitive to such a clumpy H_2 distribution as they can only probe the transparent UV sight lines, and are not able to penetrate dense clouds with $N(\text{H}_2) \gtrsim 10^{20} \text{ cm}^{-2}$ (Hoopes et al. 2004).

We next discuss the H_2 excitation mechanism in our objects. For eight objects, SHOC 137, Mrk 600, J1038+5330, Mrk 36, SBS 1222+614, Mrk 1329, Mrk 259, and Mrk 475, only one H_2 emission line, the $2.122 \mu\text{m}$ 1-0 S(1) line, is definitely detected. As a consequence, no conclusion about the H_2 excitation mechanism can be drawn for these galaxies. On the other hand, several H_2 emission lines are detected in the remaining 15 spectra of 13 objects. Comparison of the observed and theoretical ratios calculated by Black & van Dishoeck (1987), in the cases of fluorescent and collisional excitation (the last two columns at the bottom of Table 3), indicate that the observed line flux ratios are in general agreement with those predicted for fluorescent excitation. Our finding is in agreement with the conclusions of Vanzì et al. (2000) for SBS 0335–052E, of Vanzì et al. (2008) for II Zw 40 and of Izotov et al. (2009) and Izotov & Thuan (2011) for a sample of six BCDs. Those authors also found that the fluorescence process is the main excitation mechanism of H_2 lines. This conclusion appears to hold for BCDs with high-excitation spectra.

Does the H_2 emission depend on some global parameter of the galaxy? The flux of the strongest $\text{H}_2 \lambda 2.122 \mu\text{m}$ emission line does not depend on oxygen abundance (Fig. 3a). However, since H_2 is a fragile species and can be easily destroyed by stellar UV radiation, we may expect the

Table 4. [Fe II] λ 1.257 μ m, [Fe II] λ 1.644 μ m and [Fe III] λ 0.466 μ m emission-line fluxes

Object	$100 \times [\text{Fe II}]_{1.257} / \text{H}\beta$	$100 \times [\text{Fe II}]_{1.644} / \text{H}\beta$	$100 \times [\text{Fe III}]_{0.466} / \text{H}\beta$
HS 0021+1347	...	1.77 ± 0.88	1.11 ± 0.71
J0115-0051	0.66 ± 0.27	0.68 ± 0.27	0.72 ± 0.33
UM 311	1.32 ± 0.70	1.57 ± 0.76	0.76 ± 0.54
SHOC 137	...	0.41 ± 0.20	0.43 ± 0.23
Mrk 1089#1	2.25 ± 0.51	1.43 ± 0.39	0.99 ± 0.42
Mrk 1089#2	2.47 ± 0.55	1.62 ± 0.42	0.96 ± 0.41
I Zw 18	0.31 ± 0.28	...	0.56 ± 0.39
CGCG 007-025	0.80 ± 0.34	0.58 ± 0.28	0.50 ± 0.32
J1038+5330	7.69 ± 0.70	6.62 ± 0.63	1.41 ± 0.29
Haro 3#1	2.61 ± 0.91	1.53 ± 0.67	1.65 ± 0.79
Haro 3#2	1.27 ± 0.42	1.33 ± 0.43	1.13 ± 0.46
Mrk 162	2.16 ± 0.58	1.40 ± 0.45	1.24 ± 0.50
Mrk 1450	0.45 ± 0.26	0.61 ± 0.31	0.52 ± 0.31
Mrk 193	0.89 ± 0.42	0.71 ± 0.37	0.55 ± 0.40
Mrk 1315	0.18 ± 0.13	0.35 ± 0.19	0.17 ± 0.14
SBS 1222+614	0.99 ± 0.38	0.54 ± 0.27	0.72 ± 0.36
Mrk 450	0.87 ± 0.27	0.63 ± 0.22	0.81 ± 0.33
Mrk 487	0.75 ± 0.34	...	0.55 ± 0.29

H₂ flux to depend on the ionization parameter. A good observational measure of the ionization parameter is the ratio of oxygen lines [O III] λ 0.501/[O II] λ 0.373. We plot in Fig. 3b the H₂ λ 2.122 μ m/Br γ flux ratio against the [O III] λ 0.501/[O II] λ 0.373 ratio. There is a weak correlation between the two quantities in the sense that the H₂ λ 2.122 μ m/Br γ flux ratio decreases with increasing [O III] λ 0.501/[O II] λ 0.373 ratios. The linear regression is shown by the solid line. There appears to be a floor at H₂/Br γ \sim 0.05 – 0.1 with a weak statistical trend for lower H₂ 2.12 μ m/Br γ with increasing ionization parameter, suggesting an efficient destruction of H₂ molecules by the UV radiation in high-excitation H II regions.

3.3 [Fe II] line emission

The [Fe II] λ 1.257 and λ 1.644 μ m emission lines have often been used to estimate the relative importance of shock excitation and photoionization in galaxies (Moorwood & Oliva 1988; Oliva, Moorwood & Danziger 1990; Oliva et al. 2001). We have detected either one of the lines or both in 18 spectra of our galaxy sample (Table 4). The fluxes of these lines are considerably smaller in regions where photoionization dominates (\sim 1% of the H β flux) than in those where shock excitation plays the main role, such as in SN remnants. Shock models by Allen et al. (2008) with shocks propagating in the neutral gas predict the [Fe II] λ 1.257 and λ 1.644 μ m emission line fluxes to be \sim 10% – 60% that of H β .

Figs. 4ab show that the [Fe II] λ 1.257 μ m and λ 1.644 μ m to H β line ratios have the very low values of \lesssim 0.01 in high-excitation H II regions, with [O III] λ 0.501/[O II] λ 0.373 \gtrsim 3. However, in lower-excitation H II regions, the [Fe II]/H β ratios are considerably higher and they steeply increase for [O III] λ 0.501/[O II] λ 0.373 \lesssim 1. Does this mean that SN shock excitation plays an important role in galaxies with low-excitation H II regions?

Comparison of the observed flux ratios (filled and open circles) with the theoretical values from the stellar photoion-

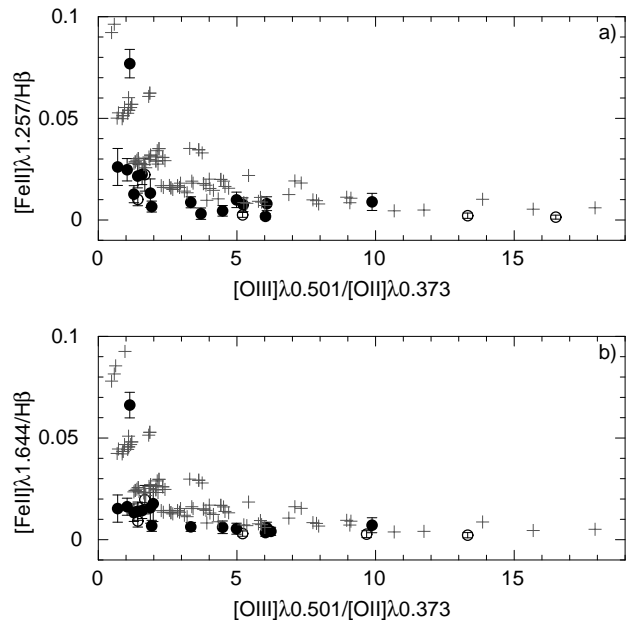


Figure 4. Dependence on the [O III] λ 0.501/[O II] λ 0.373 flux ratio of the: (a) [Fe II] λ 1.257/H β flux ratio; and (b) [Fe II] λ 1.644/H β flux ratio. The meaning of filled and open circles is the same as in Fig. 2. Theoretical flux ratios calculated with the Cloudy code (version c13.01, Ferland et al. 1998, 2013) for oxygen abundances $12 + \log \text{O}/\text{H}$ in the 7.6 – 8.3 range, and for various ionization parameters, are shown by crosses.

ization Cloudy models (crosses) in Fig. 4 shows that, even without any contribution of shock excitation from SNe, photoionization models overpredict the [Fe II] λ 1.257 and λ 1.644 μ m line fluxes by factors of \sim 1.5 – 3. An exception is the H II region J1038+5330 in the spiral galaxy NGC 3310, the most outlying object in Figs. 4ab, where the extinction-corrected [Fe II] line fluxes reach the high values of \sim 7% – 8% that of H β . However, even these high values are still in agree-

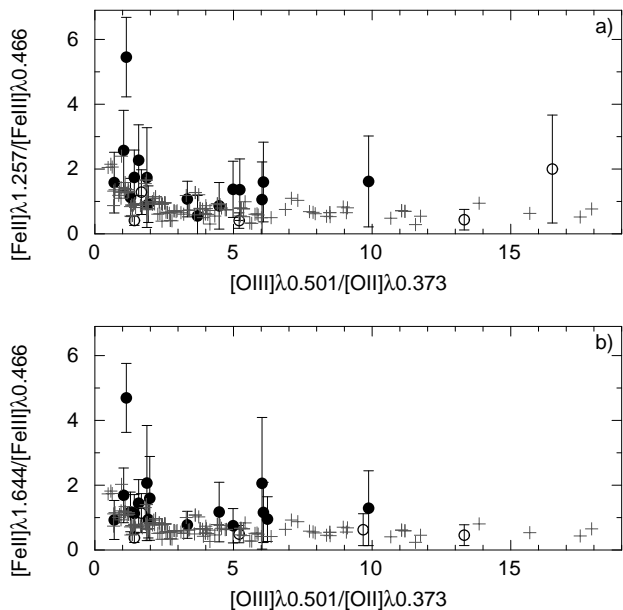


Figure 5. The dependence on the $[\text{O III}]\lambda 0.501/[\text{O II}]\lambda 0.373$ flux ratio of the : (a) $[\text{Fe II}]\lambda 1.257/[\text{Fe III}]\lambda 0.466$ flux ratio and (b) $[\text{Fe II}]\lambda 1.644/[\text{Fe III}]\lambda 0.466$ flux ratio. The meaning of filled and open circles is the same as in Fig. 2. Theoretical flux ratios calculated with the Cloudy code (version c13.01, Ferland et al. 1998, 2013) for oxygen abundances $12+\log\text{O}/\text{H}$ in the 7.6 – 8.3 range, and for various ionization parameters, are shown by crosses.

ment with the predictions of some stellar photoionization H II region models.

The relations in Fig. 4 may be affected by variations of iron abundances relative to oxygen abundances. However, the emission-line flux ratios of iron in different stages of ionization should be free of this effect. Furthermore, these ratios should also be less sensitive to iron depletion onto dust. We therefore show in Fig. 5 the $[\text{Fe II}]\lambda 1.257/[\text{Fe III}]\lambda 0.466$ and $[\text{Fe II}]\lambda 1.644/[\text{Fe III}]\lambda 0.466$ flux ratios as a function of the $[\text{O III}]\lambda 0.501/[\text{O II}]\lambda 0.373$ flux ratio. The latter is a measure, as discussed previously, of the ionization parameter. We also compare the observed ratios with theoretical predictions from Cloudy models. At variance with Fig. 4 in which the observed values are less than the predicted values, the observed values in Fig. 5 are in excess of model predictions. However, within the errors, observed and modelled flux ratios are still consistent. The only exception is again the outlier H II region J1038+5330. The $[\text{Fe II}]/[\text{Fe III}]$ flux ratios in this object cannot be reproduced by any stellar photoionization H II region model. Apparently, shocks are important contributors to the ionization and excitation of iron lines in this H II region.

Allen et al. (2008) do not give $[\text{Fe III}]\lambda 0.466$ fluxes for their shock models, which prevents us from estimating the contribution of shocks in J1038+5330. For the remaining galaxies it appears that there is no need to invoke any shock ionizing radiation. We conclude that SN shock excitation does not generally play an important role for the excitation and ionization of iron lines in BCDs. In these objects,

the presence of $[\text{Fe II}]$ lines does not necessarily imply the presence of shocks.

Some caveats regarding the model predictions should be mentioned. Allen et al. (2008) considered only shocks propagating in a neutral ISM. The situation can be quite different in our galaxies, where shocks may propagate in an ionized medium. The most sensitive ion to these differences is $[\text{Fe II}]$ and therefore the available shock model predictions for $[\text{Fe II}]$ emission may not be valid for our objects. Finally, at the present time, there is no H II region model that self-consistently treats together the effects of stellar and shock ionizing radiation. All our comparisons are based only on the superposition of stellar photoionized H II region models and shock models, calculated separately, a procedure which may not be appropriate.

3.4 He I $\lambda 2.058\mu\text{m}$ emission

The He I $\lambda 2.058\mu\text{m}$ line is one of the strongest emission lines in the *K*-band spectra of star-forming galaxies. It is observed in all objects in our sample. Since this line is emitted in the $2^1P \rightarrow 2^1S$ transition, its intensity depends on the conditions in which the permitted resonance He I Ly α $2^1P \rightarrow 1^1S$ $\lambda 584\text{\AA}$ line is scattered (Ferland 1999).

The He I Ly α $\lambda 584\text{\AA}$ photon can be converted into a $\lambda 2.058\mu\text{m}$ photon with a probability of 10^{-3} per scattering (Ferland 1980). An atom in 2^1S state can either undergo a two-photon transition to the ground state 1^1S or re-emit a $\lambda 584\text{\AA}$ photon after a $2^1S \rightarrow 2^1P$ collisional transition. Therefore, the intensity of the He I $\lambda 2.058\mu\text{m}$ line decreases with increasing dust-to-gas mass ratio due to a more efficient destruction of the $\lambda 584\text{\AA}$ photons. It can also decrease with decreasing neutral gas column density and increasing turbulent velocity because both make the $\lambda 584\text{\AA}$ photons escape the H II region more easily (Ferland 1999). Thus, the intensity of the He I $\lambda 2.058\mu\text{m}$ line can potentially be a good diagnostic for resonant line scattering in H II regions.

It is seen in Fig. 6a that the He I $2.058\mu\text{m}/\text{He I } 0.588\mu\text{m}$ flux ratio decreases with increasing $[\text{O III}]\lambda 0.501\mu\text{m}/[\text{O II}]\lambda 0.373\mu\text{m}$ flux ratio, an indicator of the ionization parameter. This dependence can be approximated by the linear maximum-likelihood relation shown by the solid black line. For comparison, we show different model dependences calculated with the Cloudy code for various neutral hydrogen column densities in the range $N(\text{H I}) = 10^{17.5} - 10^{21.5} \text{ cm}^{-2}$ [$N(\text{H I})$ increases from right to left], a turbulent velocity of 0 km s^{-1} , two values of the starburst age, 2 Myr (black dashed and dotted lines), 3 Myr (grey lines), and two values of the number of ionizing photons $Q_{\text{H}} = 10^{52} \text{ s}^{-1}$ (dotted lines) and 10^{53} s^{-1} (dashed lines). The oxygen abundance $12+\log\text{O}/\text{H} = 8.0$ is adopted for all models.

This set of Cloudy models with no turbulent velocity predicts a constant He I $2.058\mu\text{m}/\text{He I } 0.588\mu\text{m}$ flux ratio, independently of the $[\text{O III}]\lambda 0.501\mu\text{m}/[\text{O II}]\lambda 0.373\mu\text{m}$ flux ratio and the neutral hydrogen column density, and hence does not reproduce the observed trend. This is because the optical depth of the resonance transition $2^1S \rightarrow 2^1P$ in these models is always sufficiently high ($>10^3$), even in models with the lowest neutral hydrogen column density [$N(\text{H I}) = 10^{17.5} \text{ cm}^{-2}$], so that production of the He I $2.058\mu\text{m}$ photons is always efficient.

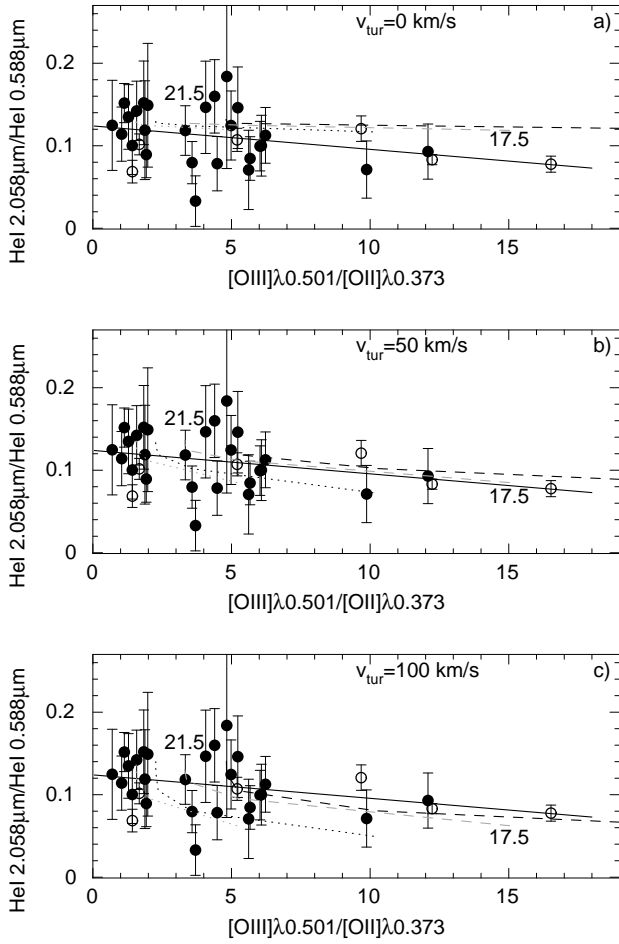


Figure 6. a) The He I 2.058/He I 0.588 flux ratio as a function of the [O III]/[O II] flux ratio. The black solid line is the maximum-likelihood fit to the data. The black dashed and dotted lines show He I 2.058/He I 0.588 flux ratios calculated with the Cloudy code for a number of ionising photons equal to 10^{53} s^{-1} (dashed line) and 10^{52} s^{-1} (dotted line), and for various values of the H I column density, varying in log scale from 17.5 to 21.5, with increments of 0.5 dex. The turbulent velocity is set to 0 km s^{-1} , while a starburst age of 2 Myr is adopted. Grey dashed and dotted lines are the same as black dashed and dotted lines, but for starburst age of 3 Myr. b) Same as a), but Cloudy models are calculated with a turbulent velocity of 50 km s^{-1} . c) Same as a), but Cloudy models are calculated with a turbulent velocity of 100 km s^{-1} .

On the other hand, models with the more realistic turbulent velocities of 50 km s^{-1} and 100 km s^{-1} , values that are observed in extragalactic H II regions (Chávez et al. 2014), do much better in reproducing the observed relation (Figs. 6bc). We thus conclude that the observed trend of the He I 2.058 μm /He I 0.588 μm flux ratio with the [O III] 0.501 μm /[O II] 0.373 μm flux ratio can be understood as due to the combined effects of turbulent motions in H II regions and a finite neutral hydrogen column density. The latter likely decreases with increasing [O III] 0.501 μm /[O II] 0.373 μm flux ratios, indicating a higher ionization parameter.

4 SUMMARY AND CONCLUSIONS

We present here near-infrared (NIR) spectroscopic observations of eighteen blue compact dwarf (BCD) galaxies and six H II regions in spiral and interacting galaxies obtained with the 3.5m APO telescope, equipped with the TripleSpec spectrograph. Two galaxies have each two different star-forming regions observed, bringing the total number of NIR spectra to twenty six. The NIR data have been supplemented by Sloan Digital Sky Survey (SDSS) spectra and some spectra obtained with the same 3.5m APO telescope and the optical DIS spectrograph. For most galaxies, the flux levels of the optical and NIR spectra are adjusted by scaling the fluxes of the [S III] $\lambda 0.907 \mu\text{m}$ emission line in the optical spectrum and the [S III] $\lambda 0.953 \mu\text{m}$ emission line in the NIR spectrum, so that their ratio is equal to the theoretical value. Only for two galaxies (those with the highest redshifts) were continua used to match the optical and NIR spectra. To increase the statistics, we have combined the present observations with our previously published NIR data on six objects, resulting in a total sample of 30 objects.

We have arrived at the following conclusions:

1. In all galaxies, except perhaps for the highest-metallicity ones, the extinction $A(V)$ derived in the optical is the same as the one derived in the NIR for the ionized gas regions traced by emission lines. The NIR emission lines of low-metallicity BCDs do not probe more extinct regions with hidden star formation as compared to the optical emission lines. For the highest-metallicity H II regions, there is a suggestion that the extinction in the NIR wavelength range corresponds to a slightly higher $A(V)$ than in the optical range.

2. We have detected molecular hydrogen emission lines in twenty three NIR spectra, i.e. in 88% of the objects in the present sample. Comparison of the observed fluxes with modelled ones suggests that the main excitation mechanism of H₂ emission in all objects is fluorescence. We find that the flux of the strongest H₂ emission line decreases when the ionization parameter increases, implying that the UV ionizing radiation of H II regions is efficient at destroying molecular hydrogen.

3. A Cloudy model with a pure stellar ionizing radiation reproduces well the observed fluxes of emission lines in both the optical and NIR ranges for all galaxies, but one. Shocks are likely present in the H II regions, but they play a minor role in the ionization. This means that the [Fe II] $\lambda 1.257$ and $\lambda 1.644 \mu\text{m}$ emission lines, often used as SN shock indicators in low-excitation high-metallicity starburst galaxies, cannot play such a role in high-excitation low-metallicity H II regions. However, we find that shocks could be important contributors to the emission of [Fe II] lines in the brightest H II region J1038+5330 of the spiral galaxy NGC 3310.

4. We find that the intensity of the He I $\lambda 2.058 \mu\text{m}$ emission line is lower in high-excitation BCDs with a lower neutral gas column density and increasing turbulent motions. These two factors favour a more efficient escape of the He I Ly α $\lambda 584 \text{Å}$ photons which are at the origin of the He I $\lambda 2.058 \mu\text{m}$ emission.

ACKNOWLEDGEMENTS

Support for this work was provided by NASA grants 1463350 and GO4-15084X. Y.I.I. is grateful to the staff of the University of Virginia for their warm hospitality. Funding for the SDSS and SDSS-II has been provided by the Alfred P. Sloan Foundation, the Participating Institutions, the National Science Foundation, the U.S. Department of Energy, the National Aeronautics and Space Administration, the Japanese Monbukagakusho, the Max Planck Society, and the Higher Education Funding Council for England. The SDSS Web Site is <http://www.sdss.org/>. The SDSS is managed by the Astrophysical Research Consortium for the Participating Institutions.

REFERENCES

- Allen M. G., Groves B. A., Dopita M. A., Sutherland R. S., Kewley L. J., 2008, *ApJS*, 178, 20
- Aller L. H., 1984, *Physics of Thermal Gaseous Nebulae*. Dordrecht: Reidel
- Black J. H., van Dishoeck E. F., 1987, *ApJ*, 322, 412
- Chávez R., Terlevich R., Terlevich E., Bresolin F., Melnick J., Plionis M., Basilakos S., 2014, *MNRAS*, 442, 3565
- Ferland G. J., 1980, *MNRAS*, 191, 243
- Ferland G. J., 1999, *ApJ*, 512, 247
- Ferland G. J., Korista K. T., Verner D. A., Ferguson J. W., Kingdon J. B., Verner E. M., 1998, *PASP*, 110, 761
- Ferland G. J., et al., 2013, *Revista Mexicana de Astronomía y Astrofísica*, 49, 137
- Guseva N. G., Izotov Y. I., Papaderos P., Fricke K. J., 2007, *A&A*, 464, 885
- Hoopes C. G., Sembach K. R., Heckman T. M., Meurer G. R., Aloisi A., Calzetti D., Leitherer C., Martin C. L., 2004, *ApJ*, 612, 825
- Hunt, L. K., Thuan, T. X., Izotov, Y. I., Sauvage, M., 2010, *ApJ*, 712, 164
- Izotov Y. I., Thuan T. X., 1998, *ApJ*, 500, 188
- Izotov Y. I., Thuan T. X., 2011, *ApJ*, 734, 82
- Izotov Y. I., Thuan T. X., Lipovetsky V. A., 1997, *ApJS*, 108, 1
- Izotov Y. I., Stasińska G., Meynet G., Guseva N. G., Thuan T. X., 2006, *A&A*, 448, 955
- Izotov Y. I., Thuan T. X., Wilson J. C., 2009, *ApJ*, 703, 1984
- Izotov Y. I., Thuan T. X., Guseva N. G., 2014, *MNRAS*, 445, 778
- Moorwood A. F. M., Oliva E., 1988, *A&A*, 203, 278
- Oliva E., Moorwood A. F. M., Danziger I. J., 1990, *A&A*, 240, 453
- Oliva E., et al., 2001, *A&A*, 369, L5
- Steffen M., Prakashavičius D., Caffau E., Ludwig H.-G., Bonifacio P., Cayrel R., Kučinskas A., Livingston W. C., 2015, *A&A*, 583, A57
- Storey P. J., Hummer D. G., 1995, *MNRAS*, 272, 41
- Thuan T. X., 2008, in *Low-metallicity star formation: from the first stars to dwarf galaxies*, ed. L. Hunt, S.C. Madden, & R. Schneider (Cambridge: Cambridge Univ. Press), 348
- Thuan T. X., Izotov Y. I., 2005, *ApJ*, 627, 739
- Thuan T. X., Lecavelier des Etangs A., Izotov Y. I., 2005, *ApJ*, 621, 269
- Vanzi L., Hunt L. K., Thuan T. X., Izotov Y. I., 2000, *A&A*, 363, 493
- Vanzi L., Hunt L. K., Thuan T. X., 2002, *A&A*, 390, 481
- Vanzi L., Cresci G., Telles E., Melnick J., 2008, *A&A*, 486, 393
- Wilson J. C., et al., 2004, *SPIE*, 5492, 1295

This paper has been typeset from a \TeX / \LaTeX file prepared by the author.